

The Galactic Magnetic Field's Effect in Star-Forming Regions

Ian W. Stephens¹, Leslie W. Looney¹, C. Darren Dowell², John E. Vaillancourt^{3,4}, Konstantinos Tassis²

ABSTRACT

We investigate the effect of the Milky Way's magnetic field in star forming regions using archived 350 μm polarization data on 52 Galactic star formation regions from the Hertz polarimeter module. The polarization angles and percentages for individual telescope beams were combined in order to produce a large-scale average for each source and for complexes of sources. In more than 80% of the sources, we find a meaningful mean magnetic field direction, implying the existence of an ordered magnetic field component at the scale of these sources. The average polarization angles were analyzed with respect to the Galactic coordinates in order to test for correlations between polarization percentage, polarization angle, intensity, and Galactic location. No correlation was found, which suggests that the magnetic field in dense molecular clouds is decoupled from the large-scale Galactic magnetic field. Finally, we show that the magnetic field directions in the complexes are consistent with a random distribution on the sky.

Subject headings: ISM: clouds — ISM: magnetic fields — polarization — stars: formation — submillimeter: ISM

1. INTRODUCTION

Magnetic fields are known to play an important role in star formation (e.g., Mouschovias & Ciolek 1999; McKee & Ostriker 2007). The line-of-sight component of the magnetic field is often measured using the Zeeman effect or Faraday rotation (e.g., Crutcher et al. 2003). The angle of the magnetic field with respect to the plane of the sky can be deduced through continuum polarization measurements. Far-infrared continuum polarization is due to emission from elongated dust grains that align perpendicularly to the magnetic field (e.g., Hildebrand 1988). For the same reason, optical light

¹Department of Astronomy, University of Illinois at Urbana-Champaign, 1002 West Green Street, Urbana, IL 61801, USA; stephen6@illinois.edu

²Jet Propulsion Laboratory, California Institute of Technology, Pasadena, CA 91109, USA

³Division of Physics, Mathematics, & Astronomy, California Institute of Technology, Pasadena, CA, 91125 USA

⁴Current address: Stratospheric Observatory for Infrared Astronomy, Universities Space Research Association, NASA Ames Research Center, MS 211-3, Moffet Field, CA 94035, USA

that has undergone partial absorption by dust grains exhibits polarization parallel to the magnetic field (e.g., Davis & Greenstein 1951).

In general the magnetic field lines of the Milky Way follow the direction of the spiral arms (often measured via Faraday rotation of pulsar signals; e.g., Han et al. 2006). Since dust polarization vectors are orthogonal to magnetic field lines, the Galactic magnetic field should induce a tendency for mapped polarization angles to be perpendicular to the Galactic disk. External galaxies also show magnetic fields following the spiral arms (e.g., Sofue et al. 1986), but on small scales (about 20 pc in the case of NGC 6946) localized processes (e.g., star formation) dominate, tangling magnetic field lines (Beck 2007).

The 350 μm Hertz polarimeter module was located at the Caltech Submillimeter Observatory and operated from 1994 to 2003. The Hertz polarimeter was well-suited for polarization measurements that probe the dense environments around forming stars, specifically clumps and cores. Since the decommissioning of Hertz, Dotson et al. (2010) have published an archive of 56 different objects, 52 of which are Galactic star forming regions. In this paper, we use this relatively large dataset of star-forming regions to calculate a single large-scale (up to an angular diameter of about 10 arcminutes) average degree of polarization (P , percentage of wave that is polarized), position angle (θ), and flux density (I) for each of the 52 star-forming Hertz datasets. The data are then explored to test whether the magnetic fields of these regions have any statistical relationship to the Galactic magnetic field.

Eritsian & Pogossian (1996) applied a similar analysis on visible polarization of 3000 stars (from the Mathewson & Ford (1970) dataset) that are in the Galactic plane. They found that the measured optical polarization angles from most stars, particularly those at further distances, are parallel to the Galactic magnetic field. Fosalba et al. (2002) found that optical polarization measurements had a sinusoidal dependence with respect to Galactic longitude.

However, we note that the observations probe very different physical regions: submillimeter observations probe dense regions ($A_V \gtrsim 30$) while optical observations probe diffuse regions ($A_V \lesssim 5$). Although dust polarization of star formation regions has been compared to the Galactic plane magnetic field before, the studies have been limited to small sample sizes. Continuum polarimetry at $\lambda = 0.8$ and 1.3 mm of approximately 10 star formation sources (at scales of $\sim 1'$) revealed no correlation for the magnetic field direction with respect to the Galactic plane (Glenn et al. 1999). On the other hand, Li et al. (2006) analyzed the dust polarization of 4 giant molecular clouds (capturing most of the clouds on scales of $\sim 10'$) at 450 μm and found that 3 of these have a significant field aligned within 15° of the Galactic plane. Our dataset probes similar regions, but we have a much larger sample size that will constrain, with much higher confidence, the relationship of the magnetic field to the Galactic plane.

Our results do not show any similar correlation for degree of polarization or angle with Galactic location. An in-depth analysis was applied for θ by binning data based on Galactic longitude and spiral arm locations, again suggesting no correlation.

This paper is organized as follows: in §2 we discuss our data and the analysis methods used. It also shows that a single polarization angle for each dataset is typically meaningful. Our results are presented in §3 and discussed in §4.

2. Observational Data and Analysis

For the 52 analyzed Hertz datasets¹, there were an average of about 90 telescope beams per object. For each telescope beam, the following values were of interest: degree of polarization (P), polarization position angle (θ), flux density (I), and the uncertainties on each. Outliers were removed for measurements with $\sigma_\theta \geq 76^\circ$, which is the 2σ point of a Gaussian distribution with a 90° full width at half maximum (most datasets have this or better). After these cuts, the average and median telescope beams per cloud were 82 and 56 respectively.

For each object, P , θ , and I values were used to calculate the Stokes parameters Q and U . These were then summed to find the large-scale average, converting back to mean Ps and θ_s . Uncertainties were propagated. A similar technique was used in Tassis et al. (2009). The mean angles were rotated from equatorial to Galactic coordinates. The spherical trigonometry for this transformation is discussed in the appendix.

2.1. Stokes Parameters, Ps , and θ_s

Since we are not able to measure circular polarization with Hertz, the Stokes parameter V is assumed to be 0; it is expected to actually be near this value. Circular polarization is also not relevant for average field direction. From I_i , P_i , and θ_i , measured at a beam location (i) in a source map, the following formulas were used to find the corresponding Q_i and U_i .

$$Q_i = I_i P_i \cos 2\theta_i \tag{1}$$

$$U_i = I_i P_i \sin 2\theta_i \tag{2}$$

From here, unweighted sums of Q_i and U_i were calculated in order to obtain $Q_{\text{tot}} = \sum Q_i$ and $U_{\text{tot}} = \sum U_i$. Similarly, an unweighted sum for intensity, $I_{\text{tot}} = \sum I_i$, was found. These quantities are not weighted by standard deviation and represent the sums as if the clouds were observed with a larger telescope beam.

By using error propagation to calculate σ_{Q_i} and σ_{U_i} , it is found:

$$\sigma_{Q_i}^2 = (P_i \sigma_{I_i} \cos 2\theta_i)^2 + (I_i \sigma_{P_i} \cos 2\theta_i)^2 + (2I_i P_i \sigma_{\theta_i} \sin 2\theta_i)^2 \tag{3}$$

¹Data available online (Dotson et al. 2010).

$$\sigma_{U_i}^2 = (P_i \sigma_{I_i} \sin 2\theta_i)^2 + (I_i \sigma_{P_i} \sin 2\theta_i)^2 + (2I_i P_i \sigma_{\theta_i} \cos 2\theta_i)^2 \quad (4)$$

The variances for Q_{tot} and U_{tot} were found by summing the variances of each beam measurement:

$$\sigma_{Q_{\text{tot}}}^2 = \sum_{i=1}^n \sigma_{Q_i}^2 \quad (5)$$

This method of calculating the standard deviation accounts for errors due to measurement in uncorrelated linear datasets. The variance for I_{tot} was calculated similarly.

From Q_{tot} , U_{tot} , and I_{tot} , $\langle P \rangle$ and $\langle \theta \rangle$ can now be calculated. $\langle P \rangle$ is seen below:

$$\langle P \rangle = \frac{\sqrt{(Q_{\text{tot}})^2 + (U_{\text{tot}})^2}}{I_{\text{tot}}} \quad (6)$$

The calculation of $\langle \theta \rangle$ is more complicated. $\langle \theta \rangle$ must always be positive, and the arctangent term does not discriminate on which Qs and Us are negative. The following formulae successfully determines the proper $\langle \theta \rangle$.

$$\langle \theta \rangle' = \begin{cases} 0.5 \arctan \frac{U_{\text{tot}}}{Q_{\text{tot}}} & : \arctan \frac{U_{\text{tot}}}{Q_{\text{tot}}} \geq 0 \\ 0.5 \left(\pi + \arctan \frac{U_{\text{tot}}}{Q_{\text{tot}}} \right) & : \arctan \frac{U_{\text{tot}}}{Q_{\text{tot}}} < 0 \end{cases} \quad (7)$$

$$\langle \theta \rangle = \begin{cases} \langle \theta \rangle' & : U_{\text{tot}} \geq 0 \\ \langle \theta \rangle' + \pi/2 & : U_{\text{tot}} < 0 \end{cases} \quad (8)$$

In order to calculate the variances for $\langle P \rangle$ and $\langle \theta \rangle$, propagation of error was used again:

$$\sigma_{\langle P \rangle}^2 = \frac{Q_{\text{tot}}^2 \sigma_{Q_{\text{tot}}}^2 + U_{\text{tot}}^2 \sigma_{U_{\text{tot}}}^2}{I_{\text{tot}}^2 (Q_{\text{tot}}^2 + U_{\text{tot}}^2)} + \frac{(Q_{\text{tot}}^2 + U_{\text{tot}}^2) \sigma_{I_{\text{tot}}}^2}{I_{\text{tot}}^4} \quad (9)$$

$$\sigma_{\langle \theta \rangle}^2 = \frac{Q_{\text{tot}}^2 \sigma_{U_{\text{tot}}}^2 + U_{\text{tot}}^2 \sigma_{Q_{\text{tot}}}^2}{4(Q_{\text{tot}}^2 + U_{\text{tot}}^2)^2} \quad (10)$$

It is important to note that equations (3), (4), (9), and (10) do not incorporate the non-diagonal (correlation) terms of covariance matrices, which are necessary for proper propagation of error. The Dotson et al. (2010) datasets do not report correlation terms from their original coordinate transformation of I , Q , and U to P and θ . Additionally, other correlation terms exist, such as observational correlations and correlations between adjacent beams. More accurate calculations of uncertainties are not motivated for the analysis and conclusions of this paper, but it should be noted that without the correlation terms, uncertainties are approximate.

Our results for a large-scale average are consistent with the polarimetric maps in Dotson et al. (2010). Although de-biasing $\langle P \rangle$, as discussed by Vaillancourt (2006), is an important part in the analysis of $\langle P \rangle$ implied by $\sigma_{\langle P \rangle}$, it was not done on these data since it does not modify the polarization angle (the primary focus for results in this paper).

The Hertz averages were analyzed in three ways: 1) investigating each of the 52 Hertz sources separately; 2) separating the sources by Galactic arm; and 3) combining near-by databases (i.e., data within 5° in Galactic longitude and less than 200 pc apart along the line of sight). The last technique reduces the amount of total datasets to 22 “complexes.”

2.2. Mean Angle Significance

To investigate whether a meaningful mean direction of the magnetic field exists or whether, instead, angles in the Hertz datasets are random (follow a uniform angle distribution) we used a Kolmogorov-Smirnov (KS) test. Out of the 52 datasets, 42 were inconsistent with a random distribution of angles at a 90% confidence level. By looking at the polarimetric maps in Dotson et al., the 10 datasets that exhibited a scatter consistent with a random distribution were maps that had poor signal-to-noise or had “circular-like” morphology (e.g., W75N). In this paper, our analysis was conducted in three ways: keeping these ten datasets; omitting these datasets; and analyzing these datasets by themselves. In all cases, we arrived at consistent conclusions.

Similarly, for the 22 complexes, 17 were inconsistent with a random distribution of angles at a 90% confidence level. Thus, the data have a meaningful large-scale average angle that is inconsistent with random processes for $>80\%$ of the sources and $>77\%$ of the complexes with 90% confidence.

A similar conclusion can also be obtained by using the normalized Stokes parameters²:

$$q' = \cos 2\theta, \quad (11)$$

$$u' = \sin 2\theta. \quad (12)$$

The values of the normalized Stokes parameters q' and u' at each pointing position within a cloud must be in the range $[-1,+1]$. Random samples drawn from a uniform distribution of angles should have an average q' and u' of 0. With a finite number of samples we can only expect that average to reach zero within some uncertainty. With approximately 56 samples per cloud, from a uniform distribution of angles we expect $\langle q' \rangle$ approximately 0 ± 0.09 . For the Hertz sample of 52 clouds, $\langle q' \rangle$ and $\langle u' \rangle$ are in the range -0.90 to 0.74 , significantly above the expectations for a uniform distribution of angles.

²The primes denote the difference between the typical definition of normalized Stokes parameters, i.e., $q = Q/I$ and $u = U/I$.

When taking the averages of the magnitudes of $\langle q' \rangle$ and $\langle u' \rangle$ for the clouds and complexes, a similar argument holds. We define $q_{\text{cloud}} = \langle |\langle q' \rangle| \rangle$ and $u_{\text{cloud}} = \langle |\langle u' \rangle| \rangle$ (i.e., the average magnitudes of $\langle q' \rangle$ and $\langle u' \rangle$) for the 52 clouds. The uncertainty due to the finite sample of 52 clouds is slightly increased from the previous paragraph. That is, for a uniform random distribution of angles we expect q_{cloud} and u_{cloud} to have a standard deviation of 0.10. The actual values for our dataset are $q_{\text{cloud}} = 0.284$ and $u_{\text{cloud}} = 0.322$, significantly larger than what could be expected from a uniform random distribution. For the 22 complexes a uniform distribution gives a standard deviation of 0.15. The actual values for our dataset are $q_{\text{complex}} = 0.196$ and $u_{\text{complex}} = 0.226$, which are both significant at an 80% confidence level.

3. Results

In this section we present an extensive examination of possible correlations between Galactic coordinates (l and b), degree of polarization ($\langle P \rangle$), Galactic polarization angle ($\langle \theta_G \rangle$; transformation from $\langle \theta \rangle$ is discussed in the appendix), and intensity ($\langle I \rangle$). Section 3.1 focuses on correlations with Galactic coordinates. Section 3.2 bins data based on Galactic arms. In both cases no relationship between location and $\langle \theta_G \rangle$ was established. Table 1 shows the data for each individual object and its associated complex; note that large clouds (e.g., OMC-1 for the fourth complex in Table 1) may be dominant for the calculated Galactic angle for a complex. Table 2 summarizes the coefficient of determination (i.e., the square of the Pearson product-moment correlation coefficient), R^2 , for most of the comparisons done. Finally, Section 3.3 examines correlation orthogonal to the Milky Way’s magnetic field.

Table 1.

Source ^a	α (2000) (h:m:s)	δ (2000) (d:m:s)	l (deg)	b (deg)	$\langle I \rangle$ (Jy)	$\sigma_{\langle I \rangle}$ (Jy)	$\langle P \rangle$ (%)	$\sigma_{\langle P \rangle}$ (%)	$\langle \theta \rangle$ (deg)	$\langle \theta_G \rangle$ (deg)	$\sigma_{\langle \theta \rangle}$ (deg)	$\langle \theta_G \rangle_{co}^b$ (deg)	$\sigma_{\langle \theta \rangle_{co}}^b$ (deg)	Spiral Arm	Dist. ^c (kpc)
W3 ¹	02:25:40.7	62:05:52	133.71	1.22	142.1	1.3	0.69	0.04	71.4	50.9	1.8	50.9	1.8	Perseus	1.95±0.04(1)
NGC 1333 ²	03:29:03.7	31:16:03	158.35	-20.56	19.8	0.3	0.36	0.43	84.9	48.1	34.3	48.1	34.3	Local	0.318±0.027(2)
L1551 ³	04:31:34.2	18:08:05	178.93	-20.05	17.2	1.6	1.23	0.62	41.6	170.9	14.3	170.9	14.3	Local	0.14±0.01(3)
IRAS 05327-0457 ⁴	05:35:14.4	-04:57:38	208.57	-19.18	19.3	0.2	3.02	0.28	143.3	80.6	2.1	143.6	0.2	Local	0.4(4)
OMC-1 ⁴	05:35:14.5	-05:22:32	208.99	-19.38	213.7	1.1	1.86	0.01	27.6	144.8	0.2			Local	0.4(4)
OMC-2 ⁴	05:35:26.7	-05:10:00	208.82	-19.25	56.8	0.7	0.54	0.05	138.8	76.1	2.7			Local	0.4(4)
OMC-3 ⁴	05:35:23.5	-05:01:32	208.68	-19.19	42.5	0.1	1.72	0.07	135.6	72.9	1.3			Local	0.4(4)
OMC-4 ⁴	05:35:08.2	-05:35:56	209.19	-19.51	24.0	2.7	1.13	0.17	167.7	104.8	4.3			Local	0.4(4)
L1641N ⁴	05:36:18.8	-06:22:11	210.06	-19.59	24.2	1.9	0.66	0.24	36.3	153.1	10.1			Local	0.4(4)
NGC 2023 ⁵	05:41:25.4	-02:18:06	206.86	-16.60	19.1	3.8	1.30	0.35	129.1	67.0	7.8	84.4	1.6	Local	0.4(4)
NGC 2024 ⁵	05:41:43.0	-01:54:22	206.53	-16.36	174.2	2.4	0.51	0.03	154.8	92.8	1.8			Local	0.4(5)
HH24MMS ⁵	05:46:08.4	-00:10:43	205.49	-14.57	10.8	1.2	1.19	0.45	90.5	28.8	10.8			Local	0.4(5)
NGC 2068 LBS 17 ⁵	05:46:28.0	-00:00:54	205.38	-14.42	8.2	0.4	0.76	0.35	49.0	167.4	13.2			Local	0.4(5)
NGC 2068 LBS 10 ⁵	05:46:50.2	00:02:01	205.38	-14.32	16.8	0.4	3.24	0.14	128.2	66.5	1.2			Local	0.4(5)
NGC 2071 ⁵	05:47:04.8	00:21:47	205.11	-14.11	44.1	1.0	0.46	0.07	147.4	85.9	4.6			Local	0.4(5)
Mon R2 ⁶	06:07:46.6	06:23:16	213.71	-12.60	140.8	3.7	0.59	0.04	30.7	147.4	1.8	164.9	2.5	Local	0.83±0.05(6)
GGD12 ⁶	06:10:50.4	-06:11:46	213.88	-11.84	95.0	3.6	0.86	0.07	90.8	27.6	2.2			Local	1(7)
S269 ⁷	06:14:36.6	13:49:35	196.45	-1.68	18.8	2.1	1.76	0.46	37.1	155.9	7.4	155.9	7.4	Perseus	3.8(8)
AFGL 961 ⁸	06:34:37.7	04:12:44	207.27	-1.81	10.7	1.0	1.14	0.36	160.9	98.6	9.0	98.6	9.0	Perseus	1.7(9)
Mon OB1 27 ⁹	06:40:58.3	10:36:54	202.30	2.53	5.8	0.7	0.52	0.46	157.0	94.4	24.9	56.4	3.7	Local	0.8(10)
Mon OB1 25 ⁹	06:41:03.7	10:15:07	202.63	2.38	16.5	4.1	1.93	0.67	116.8	54.2	9.8			Local	0.8(10)
Mon OB1 12 ⁹	06:41:06.1	09:34:09	203.24	2.08	21.6	0.1	1.42	0.14	138.7	76.1	2.9			Local	0.8(10)
NGC 2264 ⁹	06:41:10.3	09:29:27	203.32	2.06	64.6	1.1	0.57	0.04	81.1	18.6	2.2			Local	0.8(10)
ρ Oph ¹⁰	16:26:27.5	-24:23:54	353.08	16.91	46.6	4.0	1.24	0.07	161.0	29.4	1.6	27.1	2.2	Local	0.139±0.006(11)
IRAS 16293-2422 ¹⁰	16:32:22.8	-24:28:36	353.94	15.84	33.9	0.1	0.41	0.12	90.4	139.6	8.1			Local	0.178 ^{+0.018} _{-0.037} (12)
CB68 ¹¹	16:57:19.5	16:09:21	4.50	16.34	3.8	0.5	0.51	0.34	55.9	110.2	19.1	110.2	19.1	Local	0.16(13)
NGC 6334V ¹²	17:19:57.4	-35:57:46	351.16	0.70	193.9	7.0	0.21	0.05	105.9	160.7	6.2	100.0	1.1	Sagittarius	1.74±0.31(14)
NGC 6334A ¹²	17:20:19.1	-35:54:45	351.25	0.67	187.0	2.8	1.19	0.04	68.8	123.6	1.1			Sagittarius	1.74±0.31(14)
NGC 6334I ¹²	17:20:53.4	-35:47:00	351.42	0.65	487.8	7.2	0.70	0.03	36.5	91.4	1.2			Sagittarius	1.74±0.31(14)
M-0.13-0.08 ¹³	17:45:37.3	-29:05:40	359.87	-0.08	156.5	3.6	0.86	0.06	107.1	165.4	2.0	140.9	0.9	Gal. center	8(15)
Sgr A East ¹³	17:45:41.5	-29:00:09	359.95	-0.05	132.3	1.2	1.12	0.03	92.1	150.4	0.8			Gal. center	8(15)
CO 000.02-00.02 ¹³	17:45:42.1	-28:56:05	0.01	-0.01	139.7	5.8	1.08	0.03	53.5	111.8	0.7			Gal. center	8(15)
M-0.02-0.07 ¹³	17:45:51.6	-28:59:09	359.99	-0.07	127.0	2.8	1.96	0.10	80.9	139.3	1.4			Gal. center	8(15)
M+0.07-0.08 ¹³	17:46:04.3	-28:54:45	0.07	-0.07	82.3	3.0	0.58	0.08	37.5	95.8	3.9			Gal. center	8(15)

3.1. Polarization and Position Angle vs. Galactic Coordinates

Figure 1 shows four scatter plots for the 52 Galactic Hertz datasets: polarization and $\langle\theta_G\rangle$ vs. both Galactic coordinates. There is no correlation in these graphs. As expected, in plots involving the Galactic latitude b , most objects cluster around $|b| \sim 0^\circ$, as clouds lie within the Galactic plane. Those with values of b that are not near 0° are all objects in the local arm (determination of spiral arm is discussed in §3.2). Note that polarization measurements with $\sigma_{\langle P\rangle} \geq \langle P\rangle$ are not significant.

There is a sufficient gap in data points between $l \simeq 82^\circ$ and $l \simeq 196^\circ$ as well as between $l \simeq 214^\circ$ and $l \simeq 351^\circ$. Binning data into the two prevalent set of points (i.e., around $l \simeq 0^\circ$ and $l \simeq 200^\circ$) still does not yield a correlation. Furthermore, analysis of $\langle\theta_G\rangle$ and $\langle P\rangle$ vs. $\langle I\rangle$ and I_{tot} was made in attempt to see if brighter objects affect $\langle\theta_G\rangle$ and $\langle P\rangle$. No relationship was found here either.

Data were also separated into 22 complexes and analyzed in the same way as above. Figure 2 shows the same plots as Figure 1, but with the datasets reduced to 22 complexes. Again, no correlations were found in any of the relationships.

3.2. Binning Galactic l according to spiral arms

The final attempt to find correlations between location and the resulting large-scale angle averages was to plot values based on the Galactic arm in which each object is located. In order to find the corresponding object and its relevant Galactic arm, knowledge of the distance to each object is required. We used SIMBAD to confirm that the distances found in the literature for each object (see Table 1) corresponded to the correct objects. By using a graphical grid of the Milky Way (Reid et al. 2009) and basic trigonometry from distances and Galactic coordinates l and b , the correct spiral arms were ascertained. Table 3 shows the approximate distribution of data contained within each spiral arm, while Table 1 indicates the corresponding spiral arm for each object. The spiral “arms” containing the most data points are the Local Arm and the Galactic center. The arms with insufficient amounts of data were not thoroughly analyzed, though they seemed relatively random as well.

Once again, the same analysis as in Section 3.1 showed no significant correlations within spiral arm bins.

3.3. Area of avoidance

The Galactic magnetic field is thought to follow the spiral arms. Along the line of sight, the electric field of the radiation will be orthogonal to the magnetic field, i.e., pointing towards the north Galactic pole (NGP). Since $\langle\theta_G\rangle$ is measured from the NGP, it is expected that a Galactic

Table 1—Continued

Source ^a	α (2000) (h:m:s)	δ (2000) (d:m:s)	l (deg)	b (deg)	$\langle I \rangle$ (Jy)	$\sigma_{\langle I \rangle}$ (Jy)	$\langle P \rangle$ (%)	$\sigma_{\langle P \rangle}$ (%)	$\langle \theta \rangle$ (deg)	$\langle \theta_G \rangle$ (deg)	$\sigma_{\langle \theta \rangle}$ (deg)	$\langle \theta_G \rangle_{co}^b$ (deg)	$\sigma_{\langle \theta \rangle_{co}}^b$ (deg)	Spiral Arm	Dist. ^c (kpc)
M+0.11-0.08 ¹³	17:46:10.2	-28:53:06	0.11	-0.08	144.8	4.6	0.09	0.05	132.2	10.5	16.9			Gal. center	8(15)
M+0.25+0.01 ¹³	17:46:10.5	-28:42:17	0.26	0.02	135.9	11.8	0.36	0.06	93.5	151.9	4.7			Gal. center	8(15)
M+0.34+0.06 ¹³	17:46:13.2	-28:36:53	0.34	0.05	87.5	3.8	1.02	0.11	42.5	100.9	3.1			Gal. center	8(15)
Sickle (G0.18-0.04) ¹³	17:46:14.9	-28:48:03	0.19	-0.05	99.9	9.7	1.48	0.23	114.8	173.2	4.5			Gal. center	8(15)
M+0.40+0.04 ¹³	17:46:21.4	-28:35:41	0.38	0.04	75.2	2.1	1.11	0.13	160.2	38.6	3.4			Gal. center	8(15) ^d
Sgr B1 ¹³	17:46:47.2	-28:32:00	0.48	-0.01	172.5	4.1	1.00	0.04	128.4	6.9	1.1			Gal. center	8(15)
Sgr B2 ¹³	17:47:20.2	-28:23:06	0.67	-0.04	1013.2	3.5	0.36	0.01	77.1	135.6	1.0			Gal. center	8(15)
W33 C (G12.8-0.2) ¹⁴	18:14:13.4	-17:55:32	12.81	-0.20	206.3	2.3	0.21	0.03	41.7	102.9	4.3	114.0	26.2	Scutum-Crux ^e	4.5(16)
W33 A ¹⁴	18:14:38.9	-17:52:04	12.91	-0.26	83.5	1.7	0.57	0.07	129.1	10.3	3.4			Scutum-Crux ^e	4.5(16)
L483 ¹⁵	18:17:29.8	-04:39:38	24.88	5.38	9.2	0.3	0.32	0.19	163.3	45.1	16.8	45.1	16.8	Local	0.2(17)
M 17 ¹⁶	18:20:24.5	-16:13:02	15.01	-0.69	276.3	5.6	0.82	0.02	164.0	45.6	0.8	45.6	0.8	Sagittarius	1.6 ^{+0.3} _{-0.1} (18)
W43-MM1 ¹⁷	18:47:46.9	-01:54:29	30.82	-0.06	154.3	4.4	0.80	0.17	178.9	61.4	6.1	61.4	6.1	Scutum-Crux ^f	7.0 \pm 0.9(19)
G34.3+0.2 ¹⁸	18:53:18.5	01:14:59	34.26	0.15	206.6	15.6	0.51	0.16	109.3	171.9	8.8	171.9	8.8	Scutum-Crux ^g	3.7(20)
W49 A ¹⁹	19:10:13.6	09:06:17	43.17	0.01	153.1	5.7	0.45	0.03	56.7	119.0	2.0	119.0	2.0	Perseus	11.4 \pm 1.2(21)
W51 A (G49.5-0.4) ²⁰	19:23:44.0	14:30:32	49.49	-0.39	241.8	1.3	0.47	0.02	44.2	105.7	0.9	105.7	0.9	Sagittarius ^h	7 \pm 1.5(22)
IRAS 20126+4104 ²¹	20:14:29.4	41:13:34	78.13	3.62	16.6	1.6	0.49	0.37	33.0	89.2	21.4	89.2	21.4	Local	1.5 \pm 0.5(23)
W75 N ²²	20:38:36.4	42:37:35	81.87	0.78	158.8	4.1	0.22	0.09	80.0	132.3	11.0	61.1	1.0	Local ⁱ	2-3(24)(25)
DR21 ²²	20:39:01.0	42:19:31	81.68	0.54	131.0	3.2	1.05	0.03	8.0	60.2	0.8			Local ⁱ	2-3(24)(25)

Note. — Angles given represent the E-field. 8 kpc was quoted for objects in Galactic Center.

a. Numeric exponents denote the “complex” groupings for each source.

b. $\langle \theta_G \rangle$ and uncertainties for the object’s associated complex. Values listed only once for each complex.

c. Distances are from (1) Xu et al. 2006; (2) de Zeeuw et al. 1999; (3) Kenyon et al. 1994; (4) Menten et al. 2007; (5) Anthony-Twarog 1982; (6) Herbst & Racine 1976; (7) Rodriguez et. al. 1982; (8) Moffat et. al. 1979; (9) Park & Sung 2002; (10) Walker 1956; (11) Mamajek 2008; (12) Imai et al. 2007; (13) Launhardt & Henning 1997; (14) Neckel 1978; (15) distances for objects in the Galactic center were all taken to be 8 kpc; (16) Helfand et al. 2007; (17) Dame & Thaddeus 1985; (18) Povich et al. 2007; (19) Wilson et al. 1970; (20) Wink et al. 1983; (21) Gwinn et al. 1992; (22) Genzel et al. 1981; (23) Shinnaga et al. 2008; (24) Campbell et al. 1982; and (25) Odenwald & Schwartz 1993.

d. Kinematic distance is reported to be 10.0 kpc by (Walsh et al. 1997), but 8 kpc was adopted here.

e. Uncertainties may place these objects in the Near 3 kpc Arm.

f. Uncertainties may place this object in the Far 3 kpc Arm or the Long Bar.

g. Uncertainties may place this object in the Outer Arm.

h. Uncertainties may place this object in the Perseus Arm.

i. There is much discussion on the exact distance to these objects. Uncertainties may place these objects just outside Local Arm towards the Perseus Arm.

Table 2.

R^2 Comparison ^a	All Data	Complexes	$-9 < l < 82$	$196 < l < 214$	Gal. center	Local Arm
$\langle \theta_G \rangle$ vs. l	<0.01	0.06	<0.01	<0.01	0.12	<0.01
$\langle \theta_G \rangle$ vs. b	<0.01	0.13	<0.01	0.04	0.05	0.04
$\langle P \rangle$ vs. l	0.12	0.23	0.06	0.02	0.08	0.11
$\langle P \rangle$ vs. b	0.09	0.07	<0.01	<0.01	<0.01	0.08
$\langle I \rangle$ vs. l	0.16	0.23	0.02	0.18	0.36 ^b	<0.01
$\langle I \rangle$ vs. b	0.02	<0.01	0.10	0.08	<0.01	0.02
$\langle \theta_G \rangle$ vs. $\langle I \rangle$	0.02	0.02	0.03	0.03	0.02	0.03
$\langle \theta_G \rangle$ vs. I_{tot}	0.02	0.06	0.01	0.09	0.02	0.05
$\langle P \rangle$ vs. $\langle I \rangle$	0.06	0.04	0.03	0.04	0.13	0.01
$\langle P \rangle$ vs. I_{tot}	<0.01	<0.01	0.02	0.01	0.12	0.03

Note. — For the reported comparisons, $\langle \theta_G \rangle$'s were kept between 0° – 180° . Values of Galactic coordinate l that were above 350° degrees were made negative.

^aValues for each comparison is the Pearson product-moment correlation coefficient, R^2 .

^bSgr B2 has a very large intensity that is a definite outlier. Removing it causes R^2 to decrease to 0.04.

Table 3.

Spiral Arm	Number of Hertz Clouds
Perseus	4
Local	27
Sagittarius	5
Scutum-Crux	4
Galactic center	12

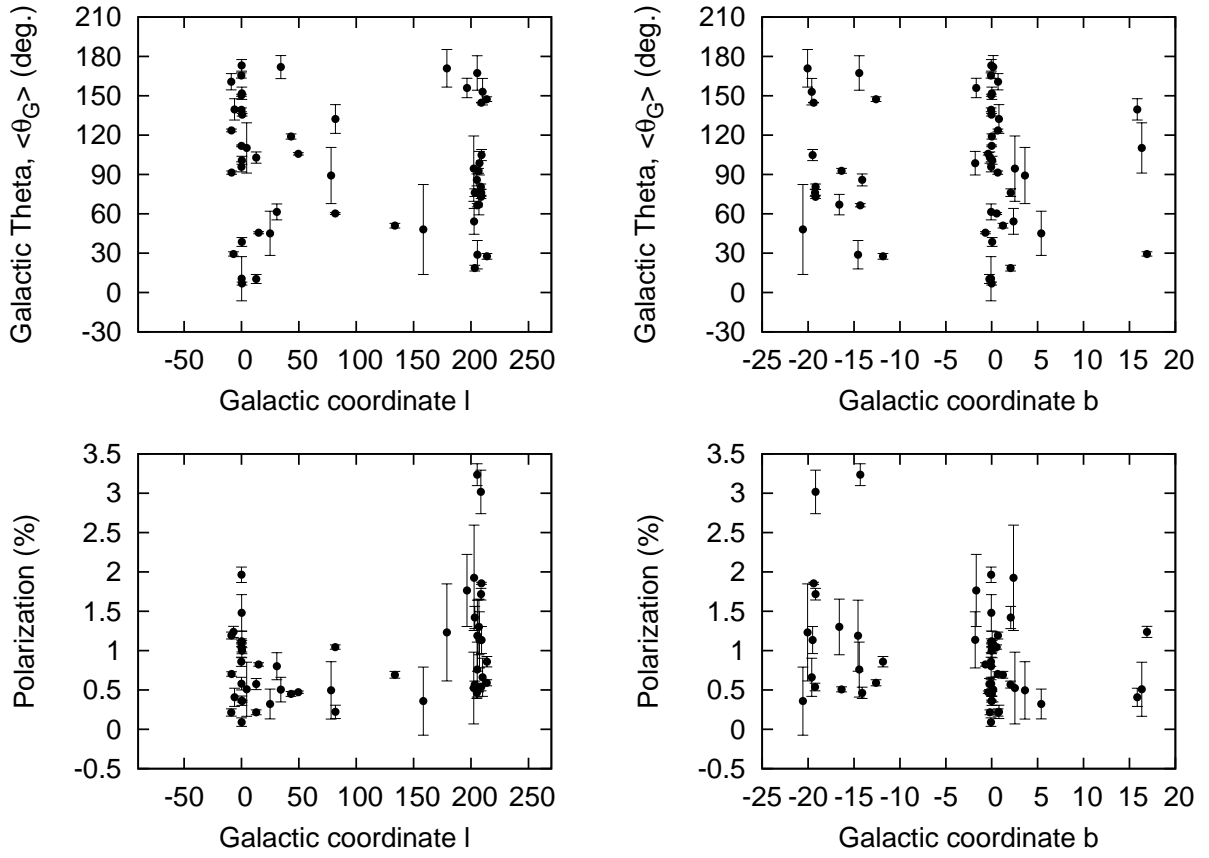


Fig. 1.— $\langle\theta_G\rangle$ and polarization vs. Galactic coordinates, all data. Error bars are 1σ .

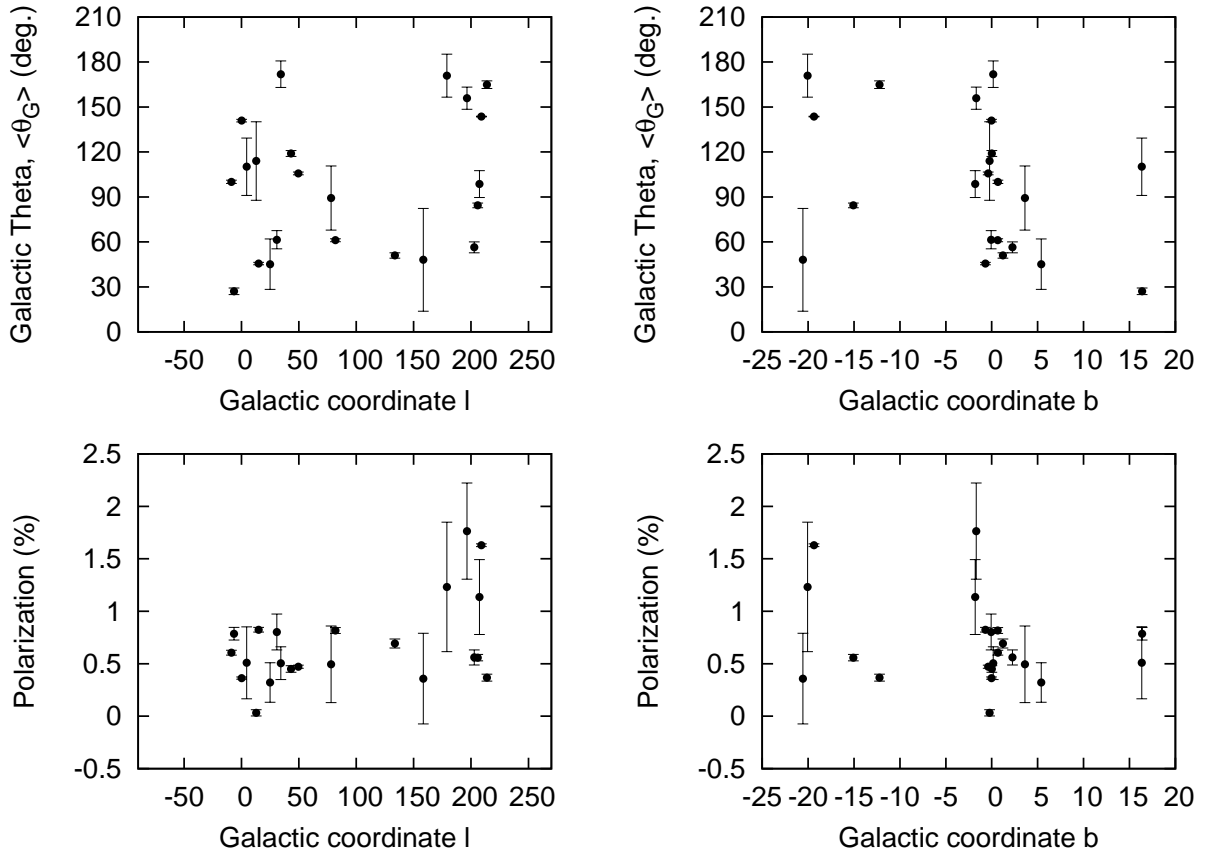


Fig. 2.— $\langle\theta_G\rangle$ and polarization vs. Galactic coordinates, complexes. Error bars are 1σ .

effect on the polarization would tend to point towards 0° and avoid 90° (i.e., orthogonal to the Milky Way’s magnetic field). However, this trend is *not* seen in Figure 3. For both large and small polarization percentages, many objects lie very near or on top of this “area of avoidance”.

3.4. Distribution of polarization angles

The Heiles catalog (Heiles 2000) has optical polarization measurements toward over 9000 stars. Those with $P > 0.2\%$ and distance >140 pc are seen in black in Figures 4. The inferred magnetic field vectors are shown in white for the 52 Hertz clouds in Figure 4a and the 22 Hertz complexes in Figure 4b. For the most part, the submillimeter angles look randomly distributed; no obvious correlation can be seen with respect to the Galactic plane. While the B-vectors of the optical data tend to be parallel to the disk of the Galaxy, the submillimeter dust polarization in star-forming regions appears to have no directional preference. A detailed comparison of Hertz data to spatially co-located Heiles data is discussed in Li et al. (2009).

It also should be noted that polarimetric maps from WMAP, which are likely dominated by dust at 94 GHz, show dust magnetic field lines parallel to the Galactic magnetic field (Hinshaw et al. 2009).

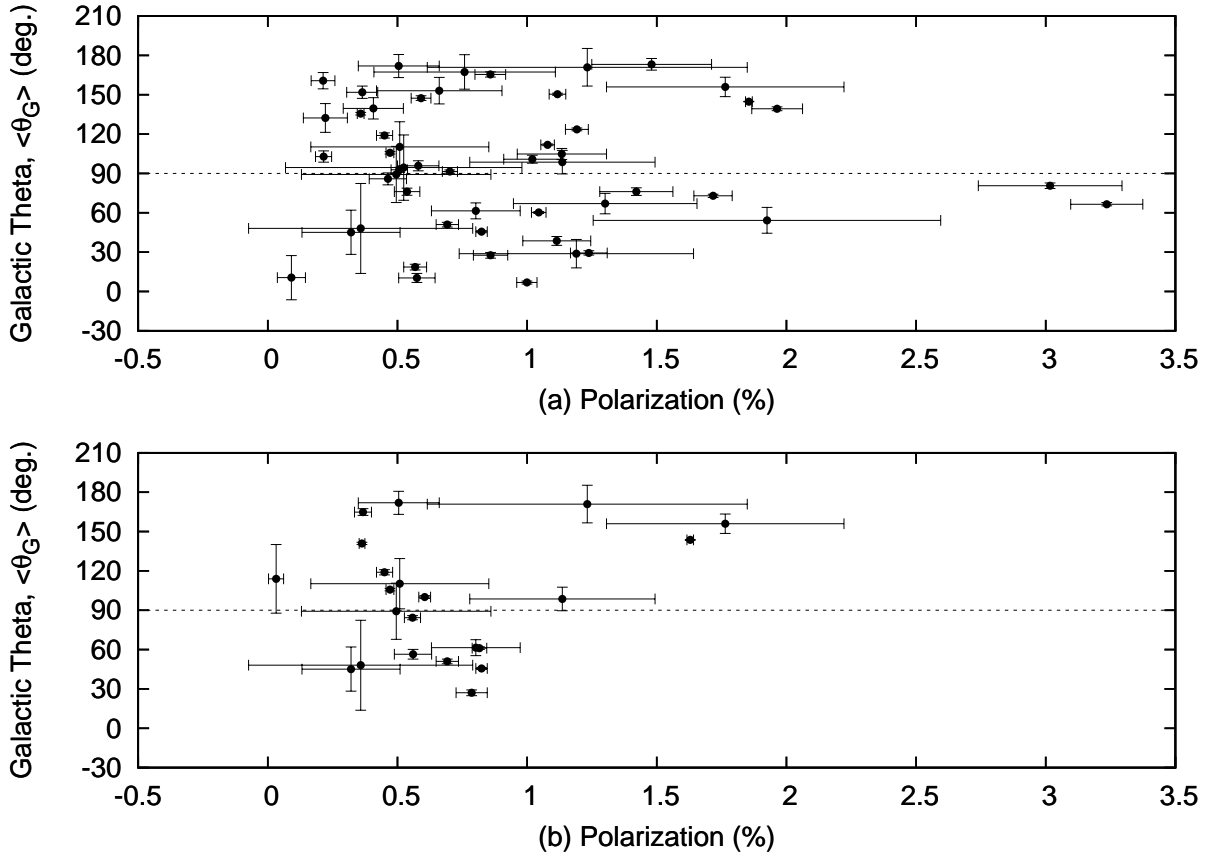


Fig. 3.— $\langle\theta_G\rangle$ vs. Polarization. (a) all data (b) complexes. Error bars are 1σ . The dashed line indicates the expected Galactic angle of avoidance at $\langle\theta_G\rangle = 90^\circ$. It does not seem that the data try to avoid this particular angle.

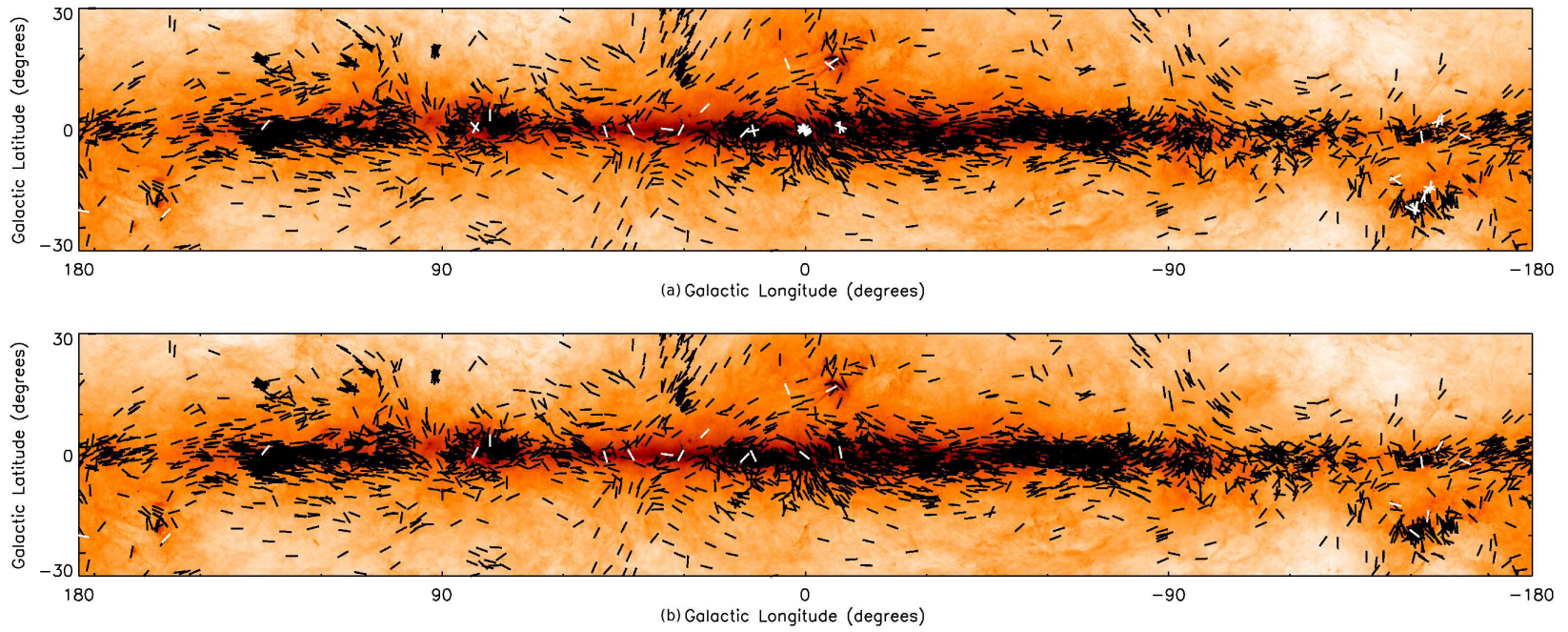


Fig. 4.— Inferred magnetic field orientations plotted in Galactic coordinates. Data from Hertz datasets (in white, with (a) all data; and (b) complexes) are shown along with background starlight polarization from the Heiles (2000) catalog (black lines, $P > 0.2\%$, distance > 140 pc). The grayscale shows the IRAS $100\ \mu\text{m}$ intensity data on a logarithmic scale (Miville-Deschênes & Lagache 2005).

A histogram of $\langle\theta_G\rangle$ for all 52 datasets is seen in Figure 5 and on inspection appears consistent with a uniform distribution. A uniform distribution for angles between 0° and 180° has standard deviation of 52.0° . Table 4 summarizes results that test whether the sources and their complexes are uniform. The standard deviations are close to 52.0° . Rows 2 and 4 are perhaps more valid because these remove datasets that appeared “random” as discussed in §2.2. A KS-test was used to compare each distribution to a uniform distribution. The p-values of these tests are shown in Table 4; high p-value indicates consistency with a uniform distribution. Since all p-values are high, there is no preferred direction in the sky.

As a comparison to the distribution of Hertz angles, a histogram of the Heiles data with $P > 0.2\%$ and distance > 140 pc is shown in Figure 6. These cuts were chosen because all Hertz datasets except one (M+0.11-0.08 at $P = 0.09\%$) fit this criteria. There is overwhelming evidence that the data are a non-uniform distribution centered around a polarization position angle of 0° . Plotting Heiles angles without cuts show similar graphs. Additional filtering was done based on larger P and extinction cuts ($E(B - V)$ in the Heiles database) because these areas generally probe denser regions. These cuts tighten the distribution around 0° .

4. Discussion and Conclusion

We have used Hertz (Dotson et al. 2010) polarization measurements in dense, star-forming clouds, to investigate whether the ordered component of the magnetic field in these clouds is correlated with location in the Galaxy. In order to obtain a single polarization percentage, angle, and intensity for each of the 52 Hertz objects (as well as the 22 complexes), the polarization information for each beam was combined into a large-scale average. With each object represented by these values, correlations with respect to location in the Galaxy (both by Galactic coordinates and spiral arm locations) were investigated.

There are three primary results for this paper:

- A meaningful polarization angle can be determined for most objects and complexes.
- No evidence was found in our data for a correlation between the polarization angle and location within the galaxy.
- The polarization angle for an object or a complex on the sky is consistent with a random distribution.

The fact that a meaningful mean direction can be identified for the magnetic field in most objects implies the existence of an ordered, large scale component of the field *within* the dense, star-forming clouds we have studied. This is consistent with the continuity of magnetic field direction on different scales within these clouds, discussed by Li et al. (2009). However, since these are star-forming clouds, feedback processes from newly formed stars can generate appreciable scatter in the

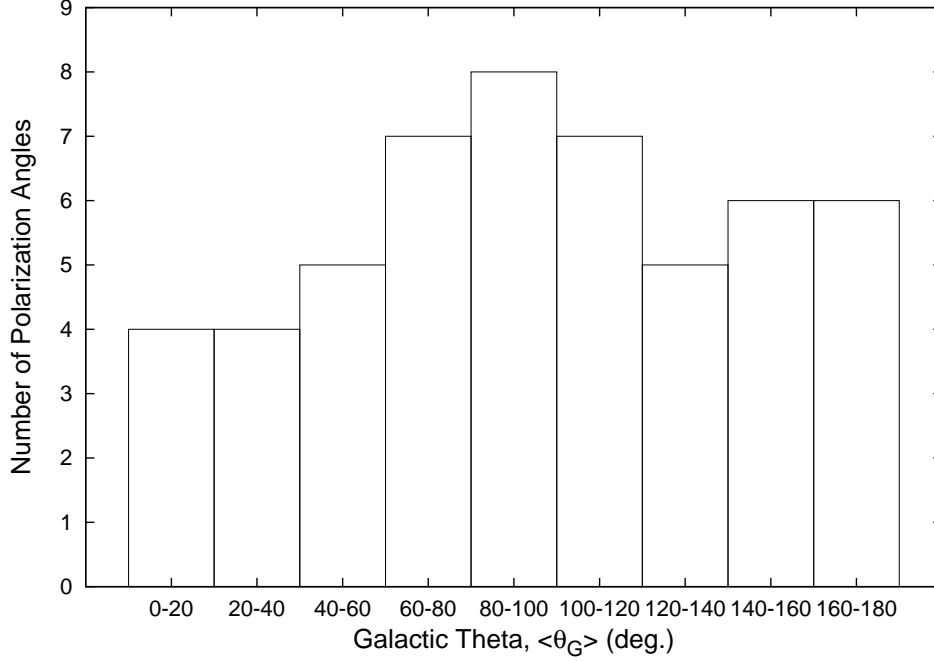


Fig. 5.— Histogram of polarization angles for the 52 datasets with 20° -wide bins.

Table 4.

Data Analyzed	σ_{dist} (deg.)	KS-test P-value
All Datasets (52)	48.6	0.69
KS-test accepted datasets (42)	47.7	0.69
All complexes (22)	45.5	0.28
KS-test accepted complexes (17)	47.5	0.51

Note. — The value in parentheses indicates the number of datasets.

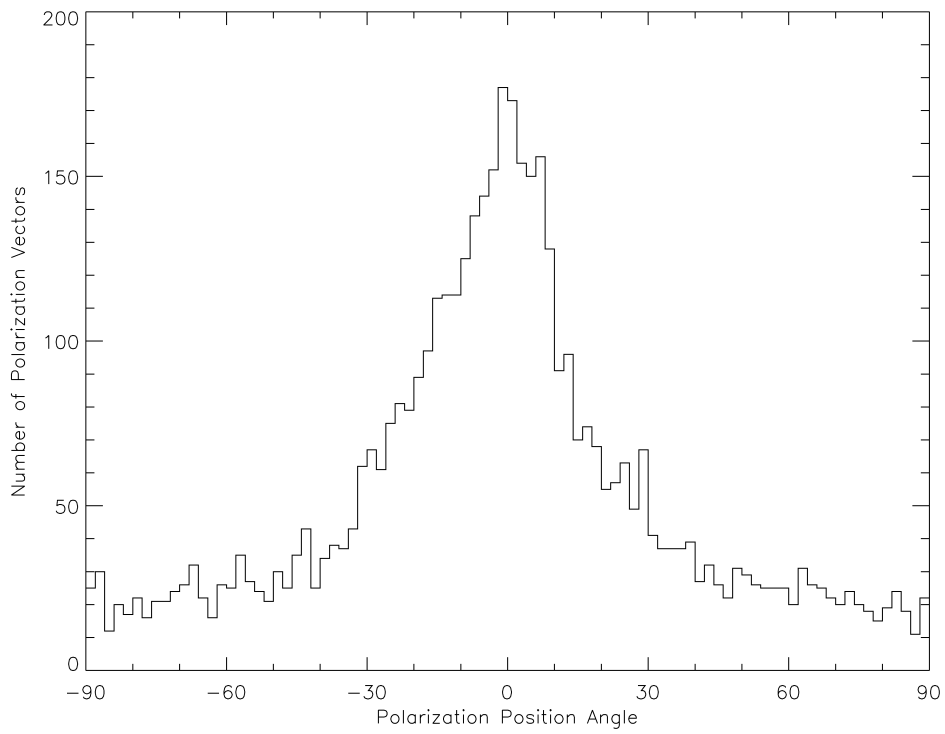


Fig. 6.— Histogram of Heiles polarization angles (with respect to Galactic coordinates) with $P > 0.2\%$ and distance > 140 pc.

magnetic field directions within each object. This may be, in part, the source of the observed angle dispersion within each dataset.

We have found that there is no significant evidence for the existence of any correlation between mean polarization angle and location, which is consistent with the results by Glenn et al. (1999) (see §1). The fact that objects do not seem to avoid polarization angles aligned with the Galaxy’s magnetic field implies that the polarization angles detected are almost entirely created by the analyzed object rather than a large-scale, external field. This suggests that complexes as a whole may become their own dynamical system that is separate from the Galaxy. The results in this paper imply that cloud cores usually have a meaningful net field (which may correlate with other cores in the same complex, (Li et al. 2009)) that has no preferred direction within the Galaxy, yet are embedded in a diffuse medium in an ordered, Galactic large-scale field.

Fish et al. (2003) did a similar analysis as this paper, but with a different methodology. They analyzed the line-of-sight magnetic fields through Zeeman splitting of OH masers in massive star-forming regions; on sub-kiloparsec scales (about 0.5 kpc), two sources often had opposite line-of-sight field directions, suggesting multiple cores in a complex tangle the magnetic fields. In some areas of the Galaxy, Fish et al. found some line-of-sight field alignment in parts of the Sagittarius Arm and Norma Arm on scales of about 2 kpc. Still, they also found no evidence for correlations of magnetic field directions in star-forming regions with the Galactic field or with the spiral arms on larger scales.

The cloud formation process involves instabilities on Galactic scales (Shetty & Ostriker 2008; Mouschovias et al. 2009; Tasker & Tan 2009), which are responsible for the accumulation of enough mass to form the clouds. At the same time, these instabilities generate turbulence in the ISM of the Galaxy. The cloud magnetic field is thus expected to decouple from the Galactic field during the cloud formation process. Stellar feedback is an additional mechanism driving the cloud magnetic field away from alignment with the Galactic field direction. These effects are likely responsible for the dichotomy between the arm/interarm regions in terms of the ratio of strengths between the ordered and tangled components of the magnetic field observed in external galaxies (Beck 2005).

Acknowledgments: Part of this work was carried out at the Jet Propulsion Laboratory, California Institute of Technology, under a contract with the National Aeronautics and Space Administration. This research has made use of the SIMBAD database, operated at CDS, Strasbourg, France. L. W. L. acknowledges support from from the National Science Foundation under grant No. AST-07-09206. We would also like to acknowledge Richard M. Crutcher for extensive discussions.

A. The Equatorial to Galactic Angle Transformation

Our goal is to convert the equatorial position angles (measured east from the north celestial pole (NCP)) to Galactic position angles (measured towards increasing longitude from the north

Galactic pole (NGP)). The location of the NCP (B1950) is exactly $l_n = 123^\circ$ and $b_n = 27.4^\circ$. By definition the NGP is at $b_{\text{ngp}} = 90^\circ$.

Let l_1 and b_1 be the location of an individual object. The rotation of the equatorial angle θ into a Galactic angle θ_G is simply the angle created at the object by lines from the NGP and NCP, as seen in Figure 7, $\angle\text{Object}$ ($\angle O$). We see the angle of arc B is always $b_{\text{ngp}} - b_n = 90^\circ - 27.4^\circ = 62.6^\circ$. Similarly, arc C is $90^\circ - b_1$, but it is unimportant with knowledge of the declination. $\angle\text{NGP}$ is $l_n - l_1$. From the law of cosines, we could use B and C to find arc A, but this is simply 90° minus the B1950 declination, δ . Therefore, $A = 90^\circ - \delta$. Now, from the law of sines we can derive an equation for $\angle O$.

$$\frac{\sin \angle O}{\sin B} = \frac{\sin \angle\text{NGP}}{\sin A} \quad (\text{A1})$$

$$\angle O = \arcsin \left[\frac{\sin(123 - l_1) \sin 62.6^\circ}{\sin(90^\circ - \delta)} \right] \quad (\text{A2})$$

$$\langle \theta_G \rangle = \angle O + \langle \theta \rangle \quad (\text{A3})$$

$\angle O$ will either be positive or negative and is added to $\langle \theta \rangle$ to get the Galactic polarization angle, $\langle \theta_G \rangle$. Since polarization vectors are “headless” (have no preferred direction), 180° is added or subtracted to the final value to make $\langle \theta_G \rangle$ between 0° and 180° . Databases such as (Mathewson & Ford 1970) and (Klare & Neckel 1977) have used this standard in the past, and this rotation method agrees with those databases to the tenth of a degree.

REFERENCES

- Anthony-Twarog, B. J. 1982, *AJ*, 87, 1213
- Beck, R. 2005, in *AIP Conf. Proc.* 784, *Magnetic fields in the Universe: From Laboratory and Stars to Primordial Structures*, ed. de Gouveia dal Pino, E. M., Lugones, G., & Lazarian, A., 343
- Beck, R. 2007, *EAS Publications Series*, 23, 19
- Campbell, M. F., Niles, D., Nawfel, R., Hawrylycz, M., Hoffmann, W. F., & Thronson, H. A., Jr. 1982, *ApJ*, 261, 550
- Crutcher, R., Heiles, C., & Troland, T. 2003, *Turbulence and Magnetic Fields in Astrophysics*, 614, 155
- Dame, T. M., & Thaddeus, P. 1985, *ApJ*, 297, 751
- Davis, L. J., & Greenstein, J. L. 1951, *ApJ*, 114, 206

- de Zeeuw, P. T., Hoogerwerf, R., de Bruijne, J. H. J., Brown, A. G. A., & Blaauw, A. 1999, *AJ*, 117, 354
- Dotson, J. L., Vaillancourt, J. E., Kirby, L., Hildebrand, R. H., & Davidson, J.A. 2010, *ApJS*, 186, 406
- Eritsian, M. H. & Pogossian, H. M. 1996, *Astrophysics*, 39, 327
- Fish, V. L., Reid, M. J., Argon, A. L., & Menten, K. M. 2003, *ApJ*, 596, 328
- Fosalba, P., Lazarian, A., Prunet, S., & Tauber, J.A., 2002, *ApJ*, 564, 762
- Genzel, R., et al. 1981, *ApJ*, 247, 1039
- Glenn, J., Walker, C. K., & Young, E. T. 1999, *ApJ*, 511, 812
- Groenewegen, M. A. T., van der Veen, W. E. C. J., & Matthews, H. E. 1998, *A&A*, 338, 491
- Gwinn, C. R., Moran, J. M., & Reid, M. J. 1992, *ApJ*, 393, 149
- Han, J. L., Manchester, R. N., Lyne, A. G., Qiao, G. J., & van Straten, W. 2006, *ApJ*, 642, 868
- Heiles, C. 2000, *AJ*, 119, 923
- Helfand, D. J., Gotthelf, E. V., Halpern, J. P., Camilo, F., Semler, D. R., Becker, R. H., & White, R. L. 2007, *ApJ*, 665, 1297
- Herbst, W., & Racine, R. 1976, *AJ*, 81, 840
- Hildebrand, R.H. 1988, *Ap. Lett. & Comm.*, 26, 263-275
- Hinshaw, B., et al. 2009, *ApJ*, 180, 225
- Imai, H., et al. 2007, *PASJ*, 59, 1107
- Kenyon, S. J., Dobrzycka, D., & Hartmann, L. 1994, *AJ*, 108, 1872
- Klare, G. & Neckel, T. 1977, *A&AS*, 27, 215
- Launhardt, R., & Henning, T. 1997, *A&A*, 326, 329
- Li, H., Griffin, G. S., Krejny, M., Novak, G., Loewenstein, R. F., Newcomb, M. G., Calisse, P. G., & Chuss, D. T. 2006, *ApJ*, 648, 340
- Li, H., Dowell, C. D., Goodman, A., Hildebrand, R., & Novak, G. 2009, *ApJ*, 704, 891
- Mamajek, E. E. 2008, *Astron. Nachr.*, 329, 10
- Mathewson, D. S., & Ford, V. L. 1970, *MmRAS*, 74, 139

- McKee, C. F. & Ostriker, E. C. 2007, *ARA&A*, 45, 565
- Menten, K. M., Reid, M. J., Forbrich, J., & Brunthaler, A. 2007, *A&A*, 474, 515
- Miville-Deschênes, M. A. & Lagache, G. 2005, *ApJSS*, 157, 302.
- Moffat, A. F. J., Jackson, P. D., & Fitzgerald, M. P., 1979, *A&AS*, 38, 197
- Mouschovias, T. C., & Ciolek, G. E. 1999, in *NATO ASIC Proc. 540: The Origin of Stars and Planetary Systems*, ed. C. J. Lada & N. D. Kylafis 305
- Mouschovias, T. C., Kunz, M. W., & Christie, D. A. 2009, *MNRAS*, 397, 14
- Neckel, T. 1978, *A&A*, 69, 5
- Odenwald S. F., & Schwartz P. R., 1993, *ApJ*, 405, 706
- Park, B.-G., & Sung, H. 2002, *AJ*, 123, 892
- Povich, M. S., Stone, J. M., Churchwell, E., Zweibel, E. G., Wolfire, M. G., Babler, B. L., Indebetouw, R., Meade, M. R., & Whitney, B. A. 2007, *ApJ*, 660, 346
- Reid, M., et al. 2009, *ApJ*, 700, 137
- Rodriguez, L. F., Carral, P., Moran, J. M., & Ho, P. T. P. 1982, *ApJ*, 260, 635
- Shetty, R., & Ostriker, E. C. 2008, *ApJ*, 684, 978
- Shinnaga, H., Phillips, T. G., Furuya, R. S., & Cesaroni, R. 2008, *ApJ*, 682, 1103
- Sofue, Y., Klein, U., Beck, R., & Wielebinski, R. 1986, *Ap&SS*, 119, 191
- Tasker, E. J., & Tan, J. C. 2009, *ApJ*, 700, 358
- Tassis K., Dowell C. D., Hildebrand R. H., Kirby L., & Vaillancourt J. E., 2009, *MNRAS*, 399, 1681
- Vaillancourt, J. E. 2006, *PASP*, 118, 1340
- Walker, M. F. 1956, *ApJS*, 2, 365
- Walsh, A. J., Hyland, A. R., Robinson, G., & Burton, M. G. 1997, *MNRAS*, 291, 261
- Wilson T.L., Mezger P.G., Gardner F.F., Milne D.K., 1970, *A&A*, 6, 364
- Wink. J. E., Wilson, T. L., & Bieging, J. H. 1983, *ApJ*, 127, 211
- Xu, Y., Reid, M.J., Zheng, X.W., & Menten, K.M. 2006, *Science*, 311, 54

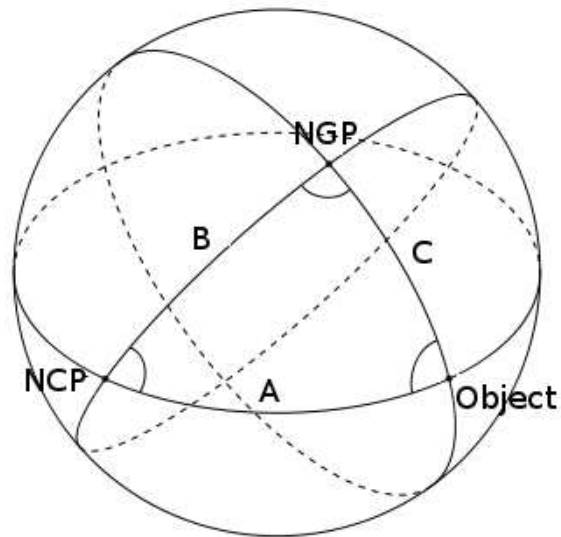


Fig. 7.— The spherical trigonometry required to convert equatorial position angles θ into Galactic position angles $\langle\theta_G\rangle$.